Riverbed sediment classification using multi-beam echo-sounder backscatter data

AliReza Amiri-Simkooei,[a] Mirjam Snellen, and Dick G. Simons
Acoustic Remote Sensing Group, Delft Institute of Earth Observation and Space Systems (DEOS), Faculty of Aerospace Engineering, Delft University of Technology, Kluyverweg 1, 2629 HS Delft, The Netherlands

(Received 31 March 2009; revised 21 July 2009; accepted 24 July 2009)

A method has recently been developed that employs multi-beam echo-sounder backscatter data to both obtain the number of sediment classes and discriminate between them by applying the Bayes decision rule to multiple hypotheses [Simons and Snellen, Appl. Acoust. **70**, 1258–1268 (2009)]. In deep water, the number of scatter pixels within the beam footprint is large enough to ensure Gaussian distributions for the backscatter strengths and to increase the discriminative power between acoustic classes. In very shallow water (<10 m), however, this number is too small. This paper presents an extension of this high-frequency methodology for these environments, together with a demonstration of its performance using backscatter data from the river Waal, The Netherlands. The objective of this work is threefold. (i) Increasing the discriminating power of the classification method: high-resolution bathymetry data allow precise bottom slope corrections for obtaining the true incident angle, and the high-resolution backscatter data reduce the statistical fluctuations via an averaging procedure. (ii) Performing a correlation analysis: the dependence of acoustic backscatter classification on sediment physical properties is verified by observing a significant correlation of 0.75 (and a disattenuated correlation of 0.90) between the classification results and sediment mean grain size. (iii) Enhancing the statistical description of the backscatter intensities: angular evolution of the *K*-distribution shape parameter indicates that the riverbed is a rough surface, in agreement with the results of the core analysis.
 [DOI: 10.1121/1.3205397]

PACS number(s): 43.30.Hw, 43.30.Xm, 43.30.Ma, 43.30.Vh [RCG] Pages: 1724–1738

I. INTRODUCTION

It is widely accepted that multi-beam echo-sounder (MBES) data can be used to measure the bathymetry of rivers, seas, and oceans. In addition, backscatter data acquired from MBES systems are employed to obtain information about the physical properties of the riverbed and seafloor. The main advantage of the method is its high spatial coverage capability at limited costs. Proper analysis and subsequent interpretation of the backscatter data are still challenging problems. The ultimate goal of acoustic classification methods is to remotely measure physical properties of the surficial sediments such as porosity, permeability, and grain-size distribution.

Methods exist that base the classification on the backscatter data from which the angular dependence has been taken out. However, complications in eliminating the angular dependence can arise, e.g., due to local bottom slopes and the unknown MBES directivity pattern. In addition, there is an intrinsic variation in the backscatter intensity with incident angle. To eliminate this angular dependence, one can, for instance, apply Lambert's law,[1] which states that the intensity of acoustic backscatter is proportional to the square of the cosine of the incident angle ($\pi/2-$grazing angle). Lambert's law does not always correctly represent the angular dependence. In fact, the statistical distribution of backscatter data changes with incident angle, and therefore removing only the mean values does not completely compensate the angular effects.

In an earlier work, a method was proposed for the classification of the seabed sediment that accounts for backscatter variability.[2] The method, based on the Bayesian decision rule, was applied to MBES backscatter data for the classification in a test area in the North Sea with well-known lithology. This method employs the backscatter strength collected at a certain incident angle instead of studying the angular behavior of the backscatter strength. The backscatter data employed are the averaged backscatter strengths per beam, i.e., obtained from averaging over backscatter strength for a large number of signal footprints or scatter pixels. The classification is performed per angle, separately from other angles, and hence it is considered to be an angle-independent method. This method needs to be adopted when applied to MBES data taken in very shallow waters.

There are two issues involved when applying a classification method such as that described in Ref. 2 to very shallow water (e.g., riverbed) areas. The shallower water depths correspond to smaller beam footprints, resulting in a smaller number of scatter pixels per beam footprint. Because the standard deviation of the averaged backscatter data is inversely proportional to the square root of the number of scatter pixels, the averaged backscatter data are subject to higher

[a]Author to whom correspondence should be addressed. Electronic mail: a.amirisimkooei@tudelft.nl. Also at: Department of Surveying Engineering, The University of Isfahan, 81744, Isfahan, Iran.

ping-to-ping variability in shallow water areas. The discriminating power between sediments will accordingly decrease. In addition, significant bottom slopes (e.g., up to 30°) exist in river environments. These will affect the incident angle and the backscatter data, and therefore the classification results. In this contribution we elaborate these two issues in detail and improve the above-mentioned classification method for a river environment. The improved classification method will be applied to a very shallow water river environment where significant slopes occur.

This paper is built up as follows. Section II briefly reviews previous work. In Sec. III, the MBES classification method proposed in Ref. 2 is briefly described. The data considered in Ref. 2 were acquired in an area where no significant slopes exist. But, for the work described in this paper the slope effects need to be accounted for. Simons and Snellen[2] used a single beam of all MBES beams available, thereby employing only a small part of the available data. Here we describe the extension of the method where almost all MBES backscatter data are accounted for in the classification. In Sec. IV we discuss our methodology to estimate the bottom slopes using the precise bathymetry data and to apply corrections to the backscatter data. Section V presents the classification results applied to the MBES data of the river Waal in The Netherlands. Extensive sediment grabbing (analyzed for grain-size distribution) is also available, which allows one to assess the performance of the classification method. The acoustic classification results are correlated with the mean grain sizes of the core data. Pearson and disattenuated correlation coefficients will be compared. We further study the problem with another class of distributions, namely, non-Rayleigh distributions. The possible application of the *K*-distribution for the classification of the data is assessed. We conclude the paper in Sec. VI.

II. BACKGROUND AND PREVIOUS WORK

Many studies of remote sediment classification use side-scan sonar systems and MBES systems[3–7] and directly compare backscatter data to the physical properties of sediments. Recent studies showing that the high-frequency (e.g., >40 kHz as we use for our classification method) acoustic backscatter data depend on the sediment physical properties in general and the grain-size distribution, in particular, can be found in Refs. 8 and 9. Our impression is that the low (insignificant) correlation coefficient (in earlier studies) between the backscatter data and the mean grain size of sediments is due to the high variability of the backscatter data, which attenuates the correlation coefficients.

Some research is going on in the field of self-organizing maps (SOMs) and artificial neural networks (ANNs) applied to the problem of seafloor classification using MBES backscatter data.[10,11] More recent studies perform seabed classification using the ANN method that preserves the backscatter angular information and incorporates both backscatter and bathymetric data.[12] The SOM is a type of ANN algorithm based on unsupervised learning. It provides a tool for visualizing the multidimensional numerical data to produce a low-dimensional map. Also similar studies are ongoing in the field of angular range analysis (ARA) using multi-beam sonar systems.[13,14] The method, based on the normalized acoustic backscatter mosaic, aims to estimate the acoustic impedance and roughness of the insonified area on the seafloor. The methods described above adjust themselves to the data without any explicit specification of the distributional form for the underlying model.[15] It is therefore difficult to statistically interpret the classification results using such methods.

The backscatter data change with the angle of incidence. The angular dependence of the backscatter data can potentially be used as a tool for classification.[16,17] A problem in this approach arises for areas where the seafloor type varies along the swath. It is therefore difficult to discriminate between the angular variation and the real seafloor type variation along the swath. In addition, the approach requires a good calibration of the MBES system, i.e., its sensitivity should be equal for all steering angles. The classification method described in Ref. 2 takes the data at a single angle and it is considered to be less sensitive to the seafloor type variation along the swath and the calibration of the MBES.

It is widely known that the backscatter data are subject to statistical fluctuations.[18–20] The classical Rayleigh distribution is not applicable to backscatter data when the deterministic number of scatterers within the signal footprint (also called size of scatter pixel or ensonified area) is not large enough and hence the central limit theorem does not hold. Non-Rayleigh distributions such as *K*, Weibull, Rayleigh mixture, or log-normal distributions occur when the conditions of the central limit theorem are violated.[20–24] Among them the *K*-distribution provides a good fit to the skewed distributions of experimental data for all sediment types.[25–28] It also offers physical insights into the backscatter data.[29,30] Previous studies have shown that the statistical characteristics of backscatter data strongly depend on the incident angle. More recent studies use angular evolution of the *K*-distribution shape parameter as a tool for seafloor characterization.[31,32]

III. ACOUSTIC CLASSIFICATION METHOD

A. Fluctuation of backscatter data

The MBES systems that typically operate at a few hundred kHz permit seafloor backscatter imaging with high resolution. The echo amplitudes (here backscatter strength) measured by the MBES can be employed for seafloor and riverbed classification. Since the signal footprint A_f (or scatter pixel) is small compared with the beam footprint for beams away from nadir, many scatter pixels are expected to fall within the footprint of the receiving beam.

It is traditionally assumed that the backscatter intensity of the ith scatter pixel in a beam, denoted by the random variable I, is exponentially distributed,[19] i.e., distributed as chi-square with two degrees of freedom. This is based on the validity of the central limit theorem where the number of scatterers N_s inside the signal footprint is large enough. The normalized amplitude $\sqrt{I}$ has a Rayleigh distribution. The corresponding backscatter strength in decibels obtained by applying $10\log_{10}$ to the intensities I has a Gumbel distribution,[33] which is a special case of the log-Weibull (or Fisher–Tippett) distribution.[34] The theory of Rayleigh distributions is not applicable to backscatter data when the number of scatterers within the signal footprint is not large enough and hence the central limit theorem does not hold (see Sec. V D).

The data employed for the classification method consist of backscatter values (in decibels) per receiver beam, i.e., backscatter values obtained from averaging over N independent scatter pixels. Such values—given for each beam angle—are corrected for propagation loss, the area A_f of the signal footprint, and the local bottom slopes. Ping-to-ping variability masks the influence of the seafloor type on the backscatter strength. The averaged backscatter value is still subject to statistical fluctuations. For large N's, the averaged backscatter is normally distributed (central limit theorem) for one sediment class. The classification method described in Ref. 2 fully employs this knowledge about the backscatter strength probability density function (PDF). It thus assumes that both N_s and N are sufficiently large.

In very shallow water (depth typically 5 m) the number of scatter pixels N is not large enough to use the central limit theorem to ensure the Gaussianity of the averaged backscatter strength. To ensure a Gaussian distribution of the backscatter strength, we here propose to use backscatter strengths averaged over small surface patches (Sec. IV). For further characterization of the riverbed sediment we may alternatively use the original backscatter intensities and apply the K-distribution explained in Sec. V D. Both will be addressed in this contribution.

B. Classification methodology

Let the backscatter intensity of the ith scatter pixel be distributed as $f_I(I)$, which is an arbitrary distribution (e.g., classically an exponential distribution). When the number N of the independent and identically distributed scatter pixels (per beam footprint) is large enough, the central limit theorem states that the averaged backscatter strength BS has a Gaussian distribution. The classification approach, described in great detail in Ref. 2 employs the averaged backscatter data at a single beam angle. Without going into detail, the method is summarized here and comprises the following steps.

Step 1 (nonlinear curve fitting): The algorithm starts by fitting r number of Gaussian PDFs, i.e., $\mathrm{BS}\sim f_{\mathrm{BS}}(\mathrm{BS})=\Sigma_{i=1}^{r} c_i N(\mathrm{BS},\mu_i,\sigma_i^2)$, to the histogram of measured backscatter strengths BS for a selected single angle. r is the number of sediment types. Each Gaussian PDF, with unknown mean μ_i and variance σ_i^2, represents one sediment type. The coefficients c_i of the linear combination of the PDFs are not known. This leads to the total number of unknown parameters as $3r$ (i.e., c_i the contribution of individual PDFs, μ_i the mean of PDFs, and σ_i the standard deviation of PDFs, $i=1,\ldots,r$).

Let the equally binned (e.g., with bin size of 0.5 dB) backscatter strength at $\mathrm{BS}_1,\ldots,\mathrm{BS}_m$ be denoted $y=[n_1,\ldots,n_m]^T$, where n_i, $i=1,\ldots,m$ is the frequency of the samples in the bin. The model of observation equation can then be written as

$$E(y)=A(x)=A(c,\mu,\sigma),\quad D(y)=Q_y, \tag{1}$$

where $A(c,\mu,\sigma)$ is expressed as an unknown linear combination of r Gaussian PDFs and the covariance matrix $Q_y=\mathrm{diag}(n_1,\ldots,n_m)$ is based on the Poisson-distributed random variables y_i's with variances n_i's. E and D are the *expectation* and *dispersion* operators, respectively.

The nonlinear least-squares problem is formulated as

$$\hat{c},\hat{\mu},\hat{\sigma}=\arg\min_{c,\mu,\sigma}\|y-A(c,\mu,\sigma)\|^2_{Q_y^{-1}}, \tag{2}$$

subject to the non-equality constraints $c\geq 0$, $\mu^l\leq\mu\leq\mu^u$, and $\sigma^l\leq\sigma\leq\sigma^u$, where $\|\cdot\|^2_{Q_y^{-1}}=(\cdot)^T Q_y^{-1}(\cdot)$ and the subscripts l and u denote the lower and upper bounds of the variables, respectively. The nonlinear least-squares subject to bounds on variables[35] is used to obtain the μ_i's and σ_i's, and the non-negative least-squares[36] is used to obtain the contributions of the individual PDFs by constraining the coefficients c_i's to be positive. (In the mathematical computer package, MATLAB one may, respectively, use lsqnonlin.m and lsqnonneg.m.)

Because in practice the number r of the sediment types is not known, it has also to be determined. The number r of Gaussian PDFs can be determined by using a goodness of fit criterion based on a chi-square distributed test statistic,

$$\chi^2=\|\hat{e}\|^2_{Q_y^{-1}}=\|y-A(\hat{c},\hat{\mu},\hat{\sigma})\|^2_{Q_y^{-1}}\sim\chi^2(m-3r), \tag{3}$$

where $\hat{e}$ is the least-squares residual vector, and $m-3r$ is the degrees of freedom. The curve fitting procedure is executed in an iterative manner for different values of r (starting from $r=1$) such that no further decrease in the test statistic is observed by increasing the number of Gaussian PDFs. For such a case and also the case when the test statistic falls below a critical value [i.e., $\chi^2_{\alpha,(m-3r)}$, with α the significance level of the test] the procedure will be stopped.

Step 2 (identification of acoustic classes): For the classification, when we know the PDF for each seafloor type i, we can apply the Bayes decision rule. We have r hypotheses H_i, $i=1,\ldots,r$, and therefore there exist r possible decisions. We choose the hypothesis that, given the backscatter observations, maximizes the likelihood function. The intersections of the r Gaussian PDFs result in r non-overlapping acceptance regions. Each interval in backscatter strength now corresponds to one acoustic class (Fig. 1).

Step 3 (assigning seafloor types): The goal is to correspond the Gaussian distributions to the grain-size distribution of the sediments. We need to assign a seafloor type to each of the r acceptance regions (acoustic classes) obtained in Step 2. There might exist different ways to approach this goal. One can, for instance, rely on the previous work,[3,4,8,9,37] where the estimated $\hat{\mu}_i$'s can directly be associated with the seafloor mean grain size. An alternative, followed in this contribution, is to use the results from the core analysis for comparison and to perform a correlation analysis afterward. Three grab samples per kilometer (a total of 30 samples for

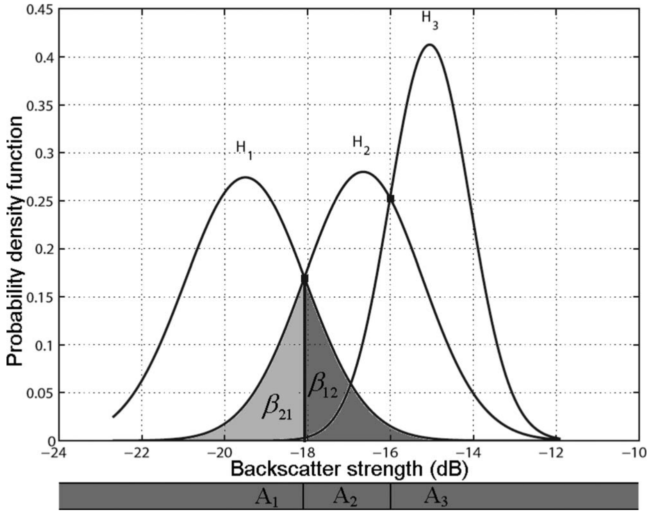

FIG. 1. Three Gaussian PDFs (H_1, H_2, and H_3) represent three sediment classes. Intersection of consecutive PDFs gives non-overlapping acceptance regions A_1, A_2, and A_3. Also indicated are examples of probability of incorrect decision β_{12} and β_{21}.

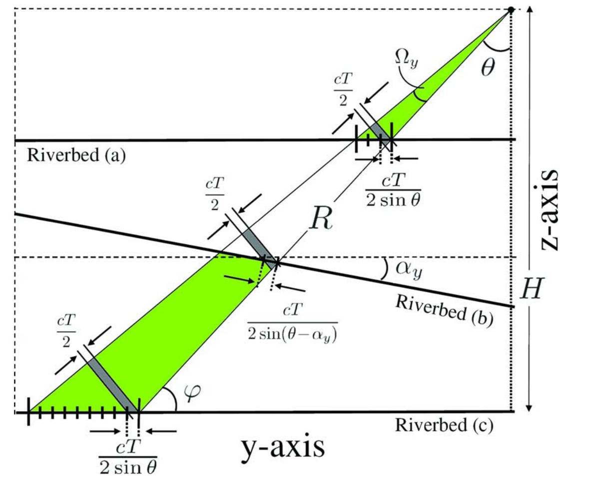

FIG. 2. (Color online) Across-track cross section (y-z plane) for signal footprint of an oblique beam for three configurations: shallow water (a), non-flat bottom (b), and deep water (c).

10 km) have been taken for such comparison (see Sec. V C).

Step 4 (quality assessment): The quality of the classification algorithm can be assessed by calculating the decision matrix of the multiple-hypothesis testing problem. This matrix contains the probabilities of correct and incorrect decisions. The decision matrix provides us with a measure for the quality of the classification method. The probability of incorrect decision is proportional to the overlap area of the Gaussian PDFs (Fig. 1). If the probability of incorrect decision decreases, the overlap area will decrease and consequently the power of the discrimination (classification) will increase.

Step 5 (presentation and mapping): This final step of the algorithm comprises the actual mapping, i.e., allocation of seafloor type (e.g., a color) to all measured backscatter strengths. As the MBES system provides a position to each backscatter strength measurement, we can map seafloor type versus position. For better presentation of the results, an interactive three-dimensional data visualization system such as FLEDERMAUS software can be used.[38] It allows, for instance, to further smooth the classification results by using a weighted moving average method.

For the analysis described above, the backscatter strengths per beam are assumed to have a Gaussian PDF. For shallow water applications N might not be sufficiently large. In addition, bottom slopes can be significant in the river environment considered in this paper. Therefore, two intermediate steps are added to the approach in Ref. 2. These steps are as follows.

Step I (correcting and averaging procedure): This step is performed before Step 1 to prepare the backscatter data (average over small patches and correct for local slopes) for the classification method described above. In shallow water environments such as rivers, the number N of scatter pixels inside the beam footprint is not large because N is proportional to the water depth [Fig. 2(a)]. The current application of the classification method, to result in the normality restoration by means of the central limit theorem, is based on the average backscatter values over the small surface patches. Each patch consists of a few beams in the across-track direction and a few pings in the along-track direction. It also allows one to apply the slope corrections to the backscatter data, namely, correction due to the changes in the area of the signal footprint and correction due to the true beam grazing angle. The details of this step are explained in Sec. IV. Therefore, for angle θ the "averaged corrected" (over patches) backscatter data will be used.

Step II (combination of different angles): This step is performed and iterated after Steps 1 and 2 to combine the results from different angles. The methodology of Simons and Snellen[2] takes observations from one single angle only. In practice, to use the full high-resolution mapping potential of the method, we may consider multiple beams and individually perform the classification. This consequently allows one to obtain a continuous map over the whole area. The classification method at angles close to nadir (e.g., $\theta=20°$), however, becomes less efficient as the backscatter values of different sediment types have values close to each other. One remedy, followed in this contribution, is to first use the backscatter data at a few low grazing angles (e.g., reference angles of $\theta=64°$, 62°, 60°) and apply the classification method. This analysis gives the number r of the sediment types, the means μ_i, the variances σ_i^2, and the coefficients c_i. The nonlinear curve fitting in Step 1 is based on the bounds on the variables. Based on this information, the curve fitting procedure is then executed and extended to all other angles ranging from $\theta=60°$, $\theta=58°, \ldots, \theta=20°$.

- For a fixed number r of the Gaussian PDFs, where r has been determined from the application of the classification method to the backscatter data of the low grazing reference angles (say, $\theta=64$, 62, 60°).
- By obtaining a good initial guess for the mean parameters, i.e., $\mu_i^0(i=1,\ldots,r)$, of the backscatter data at the angle under study. This is achieved by using the means $\mu_i(i=1,\ldots,r)$ of the reference angles and equally shifted by the differences between the mean backscatter values at the angle under study (of entire histogram) and the mean backscatter values at the reference angles.

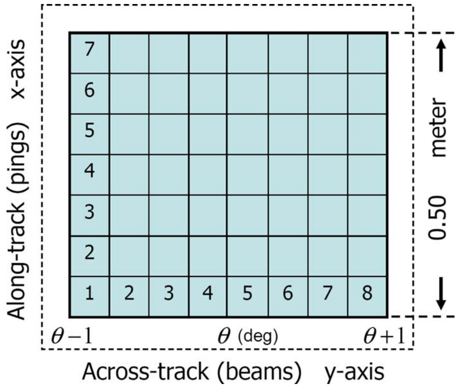

FIG. 3. (Color online) Schematic surface patch at "nominal" incident angle of θ, which consists of $m=8\times 7=56$ beams along- and cross-track directions.

- By using more strict bounds (reduce bounds) on the mean parameters $\mu_i (i=1,\ldots,r)$ for the classification of backscatter data at the angle under study (e.g., $\mu_i^l=\mu_i^0-0.5$ dB and $\mu_i^u=\mu_i^0+0.5$ dB). The bounds considered are still wide enough to compensate for the angular dependence of the statistical distributions for the backscatter data.

IV. LOCAL SLOPE CORRECTION

The significant local slopes of the riverbed will affect the classification results. To compensate for these effects, one has to estimate the along- and across-track slopes. MBESs provide detailed bathymetry information from which the local slopes can be estimated. This allows one to improve the seabed classification results by applying the corrections to the backscatter data. The literature has paid little attention to the question of how such corrections should be estimated and taken into account. We may refer, for example, to Ref. 13. We develop a methodology that compensates for the effect of bottom slopes, both in along- and across-track directions. Such effects are of high importance especially for river environments as considered in this study. Two effects are discussed: (1) correction due to the changes in the ensonified area (signal footprint) to which the backscatter data refers and (2) correction due to the true beam grazing angle. Both corrections can be applied when the along- and across-track slopes of the seafloor (riverbed) are available. The least-squares method is employed to estimate the local slopes using the precise bathymetry data.

A. Estimation of slopes

A discrete surface patch $z_i=f(x_i,y_i)$, $i=1,\ldots,m$ includes a few angles around the central beam angle (e.g., with deviation of 1°), where the angular dependence of the statistical distribution of the backscatter data is negligible. Also, because the ping rate is high (40 Hz), we may in addition include a set of neighboring pings to make a surface patch and hence to be able to estimate the along- and across-track slopes. This results in a window (e.g., 0.5×0.5 m^2) that contains, say, $m=56$ beams (Fig. 3). The average backscatter data and the average depth in this small patch will be used. Using this strategy to divide the area under survey into small surface patches and to use the average backscatter values, (a) one can compute the along- and across-track slopes and correct for the true grazing angle and the backscatter data; (b) One can assure that the normality assumption is achieved by means of the central limit theorem. This is a prerequisite for using the classification method (see Sec. III). (c) One can decrease the variance and hence increase the discriminating power between sediments. This makes the classification method more discriminative.

A bi-quadratic function consisting of six unknown coefficients is used to model (estimate) the surface patch. This subsequently allows one to obtain the along-track (x) and across-track (y) slopes

$$z=f(x,y)=a_0+a_1x+a_2y+a_3x^2+a_4y^2+a_5xy. \qquad (4)$$

The least-squares method can be used to estimate the parameters of the polynomial, and a procedure called "data snooping"[39] can be used to test for the presence of outliers in the bathymetry data (see below). When the local surface is small enough, further simplification of $f(x,y)$ is possible by using a plane instead of a bi-quadratic polynomial ($a_3=a_4=a_5=0$). The subsequent formulations can thus be simplified accordingly.

For the linear model of observation equations $E(z)=Aa$, the least-squares estimate of the vector of unknown coefficients $a=[a_0,\ldots,a_5]^T$ is

$$\hat{a}=(A^TQ_z^{-1}A)^{-1}A^TQ_z^{-1}z, \qquad (5)$$

where A is the known $m\times 6$ design matrix (its ith row is $A_i=[1\ x_i\ y_i\ x_i^2\ y_i^2\ x_iy_i]$), $z=[z_1,\ldots,z_m]^T$ is an m-vector of depth measurements, and $Q_z=\sigma^2 I$ is the covariance matrix of z, with σ^2 the variance of the data and I an identity matrix. Note that for this special structure of $Q_z=\sigma^2 I$ (independent and identically distributed errors), Eq. (5) simplifies to $\hat{a}=(A^TA)^{-1}A^Tz$. It indicates that the unknown coefficients a can be estimated independent of the (un)known variance of the data. The least-squares estimate of the variance component is $\hat{\sigma}^2=\hat{e}^T\hat{e}/(m-6)$, where $\hat{e}=A\hat{a}-z$ is the m-vector of the least-squares residual.[40] The covariance matrix of the unknown coefficients a is given as: $Q_{\hat{a}}=\hat{\sigma}^2(A^TA)^{-1}$. Also the covariance matrix of the residuals is $Q_{\hat{e}}=\hat{\sigma}^2(I-A(A^TA)^{-1}A)$.

The data snooping procedure[39] for the detection, identification, and adaptation of possible outliers and anomalies in the measurements can be applied in an iterative manner to screen the observations from the presence of such errors. The normalized entries of the residual vector $\hat{e}$, i.e., $\hat{w}_i=\hat{e}_i/\sigma_{\hat{e}_i}$ (i runs from 1 to m), is a test statistic used for data snooping. In this statistic, $\sigma_{\hat{e}_i}=(Q_{\hat{e}})_{ii}^{1/2}$ is the standard deviation of the least-squares residuals obtained as the square root of the ith diagonal entry of $Q_{\hat{e}}$. The test statistic w_i has a standard normal distribution when σ^2 is known. It has a Student t distribution when σ^2 is unknown. When the test for observation i is rejected, one may conclude that observation i is affected by some extraordinary large errors. By letting i run from 1 to m, one can screen the data on the presence of potential outliers in the individual observations. The test statistic $w_{\max}$ (one value out of m values: $w_{\max}=\max(w_i)$, $i=1,\ldots,m$) that has the largest (in absolute sense) value refers to the observation which is most likely corrupted with a outlier. The corresponding observation is excluded from the list of observations and the same procedure is applied for identifying yet other potential outliers.

The estimated bathymetry data, which express the estimated local surface, are $\hat{z}=\hat{f}(x,y)=A\hat{a}$. At point (x,y) the partial derivatives of $\hat{z}=\hat{f}(x,y)$ with respect to x, $\hat{a}_x=\hat{f}_x(x,y)=\hat{a}_1+2\hat{a}_3x+\hat{a}_5y$, and with respect to y, $\hat{a}_y=\hat{f}_y(x,y)=\hat{a}_2+2\hat{a}_4y+\hat{a}_5x$, give the tangent planes (or slope) at these two directions. We may now obtain the average local slopes at the discrete points $1,\ldots,m$ as

$$\hat{a}_x=\frac{1}{m}\sum_{i=1}^{m}\hat{f}_x(x_i,y_i), \quad \hat{a}_y=\frac{1}{m}\sum_{i=1}^{m}\hat{f}_y(x_i,y_i), \tag{6}$$

for along- and across-track, respectively. The average angles α_x and α_y that the tangent plane makes with the positive x and y axes are $\alpha_x=\tan^{-1}a_x$ and $\alpha_y=\tan^{-1}a_y$, respectively. The least-squares method can provide us with the precision of the estimates. The covariance matrix of the estimates $\hat{a}$ is $Q_{\hat{a}}=(A^TQ_z^{-1}A)^{-1}$. One can thus obtain the standard deviation of a_x and a_y, and hence the standard deviation of α_x and α_y.

Finally, a practical comment on the coordinates transformation is in order. For the local surfaces usually the geographic coordinates north (N) and east (E) in the Universal Transverse Mercator (UTM) coordinate system are available and not directly the vessel frame coordinates x and y. These two sets of coordinate systems can be transformed to each other using the transformation

$$\begin{bmatrix} x \\ y \end{bmatrix}=\begin{bmatrix} \cos\alpha & \sin\alpha \\ -\sin\alpha & \cos\alpha \end{bmatrix}\begin{bmatrix} N \\ E \end{bmatrix}, \tag{7}$$

where α is the heading angle of the vessel. One way to estimate the along- and across-track slopes is to transform the coordinates to the vessel frame system using Eq. (7) and use the previous formulation. An alternative is to estimate the slopes in the E-N system (i.e., $\hat{a}_N=\hat{a}'_1+2\hat{a}'_3N+\hat{a}'_5E$ and $\hat{a}_E=\hat{a}'_2+2\hat{a}'_4E+\hat{a}'_5N$) and then transform them into the x-y system using (Appendix A)

$$\hat{a}_x=\hat{a}_N\cos\alpha+\hat{a}_E\sin\alpha,$$

$$\hat{a}_y=-\hat{a}_N\sin\alpha+\hat{a}_E\cos\alpha. \tag{8}$$

This equation is similar to the transformation of Eq. (7). Therefore, one can either transform the coordinates first and then estimate the slopes in the vessel frame system, or estimate the slopes first and then transform them using Eq. (8).

B. Grazing angle correction

Suppose that the local surface is estimated as $\hat{z}=\hat{f}(x,y)$. The average local slopes $\hat{a}_x$ and $\hat{a}_y$ of the surface are given by Eq. (6). The normal vector to this surface patch is (the gradient of the surface)

$$\vec{n}=[\hat{a}_x\ \hat{a}_y\ -1]^T=[\tan\alpha_x\ \tan\alpha_y\ -1]^T. \tag{9}$$

On the other hand, the nominal receiving-beam direction, which is based on the flat surface in the z-y plane, is $\vec{m}=[0 -\cos\varphi\ \sin\varphi]^T=[0 -\sin\theta\ \cos\theta]^T$, where θ is the nominal incident angle and $\varphi=\pi/2-\theta$ is the grazing angle (see Fig. 2). The angle between the two vectors $\vec{n}$ and $\vec{m}$ is the true incident angle and is given as

$$\cos\theta_t=\frac{\vec{n}\cdot\vec{m}}{\|\vec{n}\|\|\vec{m}\|}=\frac{\sin\varphi+a_y\cos\varphi}{\sqrt{1+a_x^2+a_y^2}}. \tag{10}$$

This equation can thus be used to obtain the true grazing angle ($\varphi_t=90-\theta_t$) when both the along- and across-track slopes are available. In a special case when $a_x=0$ it follows, with $a_y=\tan\alpha_y$, from Eq. (10) that $\theta_t=90-(\varphi+\alpha_y)$ and hence $\varphi_t=\varphi+\alpha_y$.

C. Backscatter correction

Another correction due to the local slopes a_x and a_y is the fact that the signal footprint (ensonified area) will change if the surface is not flat. We now aim to correct the backscatter data for the local bottom slopes. The backscattering strength is obtained from the echo signal using the sonar equation[1]

$$\mathrm{BS}(\theta)=\mathrm{EL}(\theta)-\mathrm{SL}(\theta)+2\mathrm{TL}-10\log A_f(\theta), \tag{11}$$

where EL is the echo level, SL is the source level, TL is the transmission loss, and A_f is the true area of the signal footprint. The relation between true area A_f and nominal area A'_f (based on a flat surface) is $A_f=\lambda A'_f$, where λ is a scaling factor. This results in $\log A_f(\theta)=\log A'_f(\theta)+\log\lambda(\theta)$. The correction $C=-10\log\lambda(\theta)$ is then obtained as a function of local slopes in along- and across-track directions.

For angles away from, nadir the area A'_f is given as[1]

$$A'_f(\theta)=\frac{cTR\Omega_x}{2\sin\theta}=\frac{cTR\Omega_x}{2\cos\varphi}, \tag{12}$$

where Ω_x is the beam aperture in the along-track direction and φ is the grazing angle. The term $\delta_y=cT/2\sin\theta$ is the across-track resolution (size of the scatter pixel) of the backscatter imaging, and $\delta_x=R\Omega_x$ is the along-track resolution. When there exist significant bottom slopes, the area of the signal footprint may be modified to (Fig. 2)

$$A_f(\theta)=\frac{cTR\Omega_x}{2\sin(\theta-\alpha_y)\cos\alpha_x}. \tag{13}$$

The term $\cos\alpha_x$ in the denominator of the preceding equation indicates that the area is always larger in the along-track direction. This however, does not hold for the across-track direction as it depends on θ. The correction $C=-10\log\lambda(\theta)$ is then

$$C=10\log\left(\frac{\sin(\theta-\alpha_y)\cos\alpha_x}{\sin\theta}\right), \tag{14}$$

which is expressed in decibels. We now assume that the local slopes α_x and α_y are uncorrelated and have the same standard deviation σ_α. Application of the error propagation law[41] to the linearized form of Eq. (14) gives the standard deviation of the correction as

$$\sigma_C = \frac{10\ \sigma_\alpha}{\ln 10}(\tan^2(\varphi + \alpha_y) + \tan^2\ \alpha_x)^{1/2}, \tag{15}$$

which is obtained in decibels. One can further simplify this equation by using the approximate values of $\alpha_x=0$ and $\alpha_y=0$ as

$$\sigma_C = \frac{10 \cot \theta \sigma_\alpha}{\ln 10}. \tag{16}$$

Equation (16) shows that the correction is not significant at low grazing angles, but it may not be neglected at high grazing angles.

For the near nadir beams (high grazing angles with $\theta \approx 0$), the area A'_f of a flat surface is given as

$$A'_f = R^2 \Omega_x \Omega_y, \tag{17}$$

where Ω_y is the beam aperture in the across-track direction. With the presence of bottom slopes, the area A_f at normal incidence is modified as

$$A_f = \frac{R^2 \Omega_x \Omega_y}{\cos \alpha_x \cos \alpha_y}. \tag{18}$$

V. RESULTS AND DISCUSSIONS

A. Experiment description

The river Waal is the main distributary branch of river Rhine flowing to the central Netherlands for about 80 km. It is a major river that serves as the main waterway connecting the Rotterdam harbor and Germany for commercial activities. Along several parts of this river, the bottom is subsiding. Since the subsidence varies along the river, dangerous shoals can occur. Appropriate sediment suppletion—it is a stable layer of concrete blocks—is planned to counteract the subsidence and to keep the riverbed more stable. To monitor the suppletion effectiveness, regular MBES measurements are planned, allowing for simultaneous estimation of bathymetry and sediment composition.

In October 2007, as a first step, MBES measurements were acquired at the Waal, accompanied with extensive sediment grabbing. The MBES used for the measurements is a Kongsberg EM3002, which was hull-mounted at a depth of 70 cm in the water. It typically works at a frequency of 300 kHz for shallow water (1–150 m). The depths of the area under survey range from 2 to 10 m. The EM3002 system used has a single sonar head with left and right transducers. Other technical specifications of this system are as follows: (1) The pulse length is 150 μs. (2) The maximum number of beams per ping is 254. (3) The maximum ping rate is 40 Hz. (4) The maximum angular coverage is 130°. (5) The beamwidth is $1.5° \times 1.5°$ at nadir. (6) The beam pattern is equidistant or equiangular. (7) The transducer geometry is mills cross.

The bathymetry of this study area is shown in Fig. 4. Except for the flat area (sediment suppletion to prevent deformation in the outer part of the bend) in the middle of the area, the river exhibits significant bottom slopes. This section presents the results of the acoustic sediment classification based on the methodology developed in Secs. IV and III. To assess the MBES classification results, a comparison is made with the analysis of the grab samples.

B. Acoustic classification results

We now apply the classification method of Sec. III to the above-described set of backscatter data. Figure 5 shows the histogram along with its best Gaussian fit for the original backscatter values at $\theta=60°$ and $\theta=62°$. The two Gaussian PDFs indicate that there exist two sediment types for the riverbed. Note that a third PDF was also found which has a small contribution of 0.3%. This third PDF is likely due to the heterogenity in the sediments or the violation of the normality assumption because we deal with a small number of scatter pixels per beam footprint. One may consider to apply the classification method based on these results.

There are, however, two issues that need to be addressed: (1) water depths are very shallow and (2) significant bottom slopes exist. The low depth results in a small number of scatterers within the signal footprint (N_s is low) and a small number of scatter pixels per beam footprint (N is low). In both cases, the central limit theorem is not valid, and consequently neither is the normality assumption of the backscatter data. These will affect the classification results. Also, the lower water depths correspond to higher ping-to-ping variability and hence higher fluctuation for backscatter data. Therefore, the discriminating power of the classification decreases as the two Gaussian PDFs are highly overlapped (Fig. 5). The second issue is the bottom slopes, which can significantly affect the backscatter data and the grazing angle.

One way out of this dilemma is to increase the number of samples for each beam considered (Secs. IV and III). This is achieved by including more angles around the central beam angle (e.g., with deviation of 1° as $\theta - 1° < \theta < \theta + 1°$). For such close angles, the angular dependence of the backscatter distribution can be ignored. One can also average over a few consecutive pings (e.g., 7 pings) because the ping rate (40 Hz) is high in shallow water. This results in a small surface patch that contains, say, 56 beams (Fig. 3). The averaged corrected (over patches) backscatter data will then be used.

The number of bottom types is unknown and needs to be determined according to the method described in Sec. III B. This is achieved by increasing the number of Gaussian functions to well describe the histogram of the averaged backscatter strength values after applying the slope corrections and averaging over the small patches. Figure 6 shows a plot of test statistic χ^2 in Eq. (3) versus the number r of the Gaussian PDFs. The value of r at which either the test statistic falls below the critical value or no further significant decrease in test statistic is obtained is the optimal value for r. This value is set to be $r=3$ (Fig. 6), which is the "estimated" number of bottom types based on the acoustic data.

Figure 7 shows the histogram and its best Gaussian fit for the averaged backscatter values. Three Gaussian PDFs, indicating three acoustic classes, are identified. The previously detected small PDF (Fig. 5) is averaged out over the

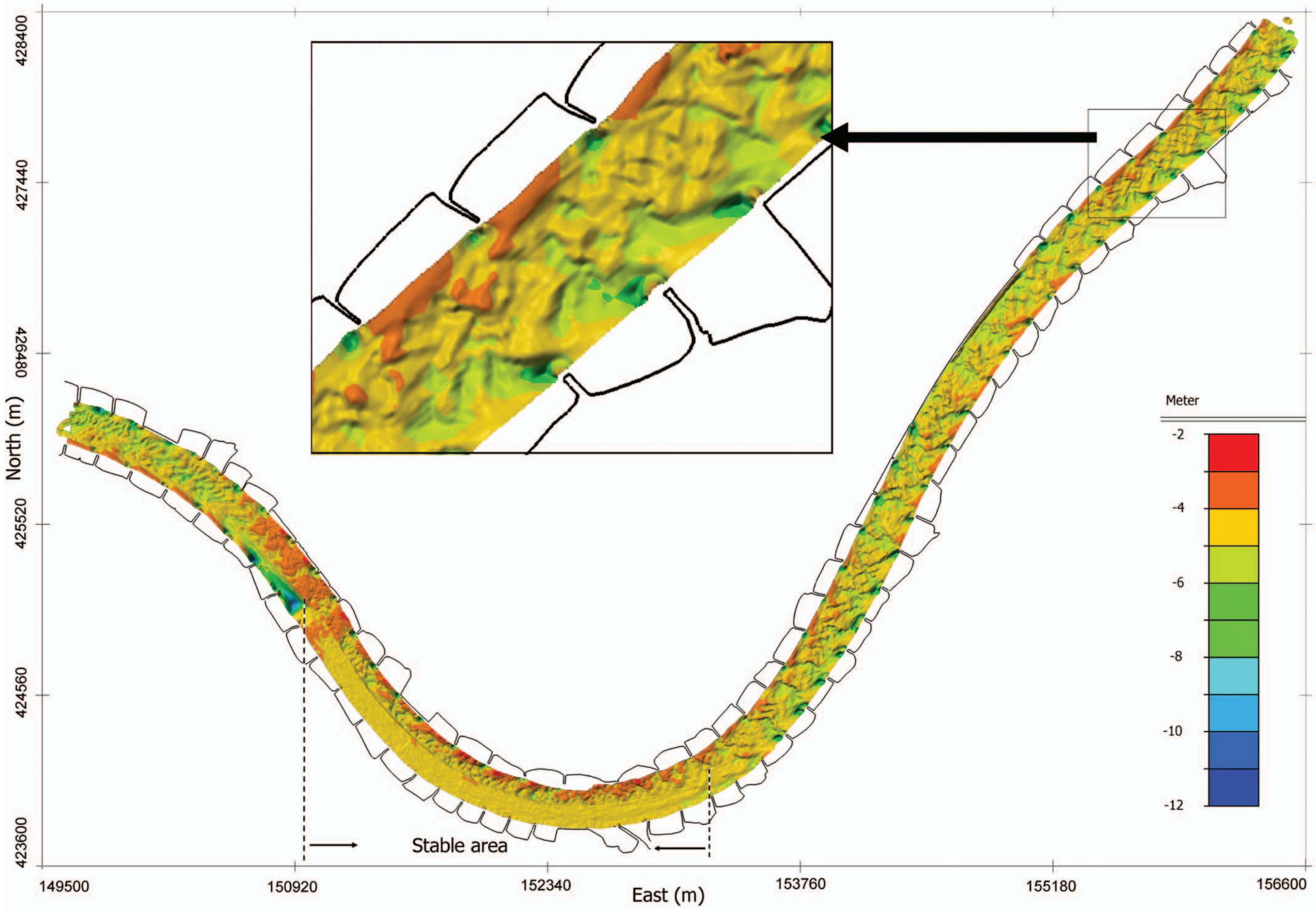

FIG. 4. Bathymetry map of river Waal, The Netherlands; km 920–930 [km 0 refers to a bridge in Constance, Switzerland (Ref. 42)].

small patches and it is not detectable anymore. However, a new PDF (a third one) is now detected and the Gaussian PDF distributions are better separated. The histograms are more peaked than those in Fig. 5, indicating lower variance and higher discriminating power. Also, the left tail of the histogram is now longer (left-skewed), indicating that the mass of the distribution is concentrated on the right hand side. The contributions of the PDFs are roughly 5%, 40%, and 55%. It is worthwile mentioning that the classification method is in-

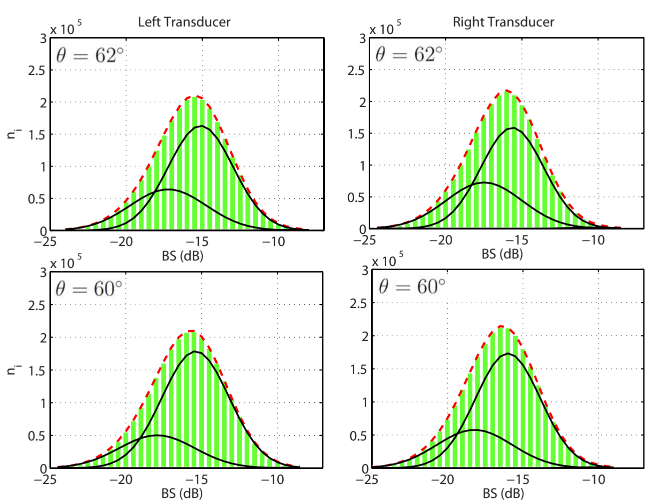

FIG. 5. (Color online) Histograms (light bar) of original measured backscatter data, its three Gaussians (solid line), and its best fit (dashed line) at angles θ=62° (top) and θ=60° (bottom) over the whole area; left and right transducers; number of Gaussians r=3 (third PDF is very small and located at μ_3=−10 dB).

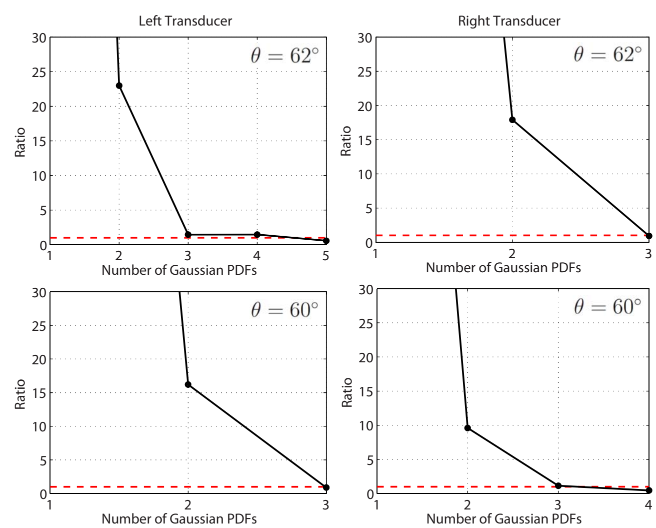

FIG. 6. (Color online) Normalized (ratio of test statistics to their corresponding critical values) chi-squared test statistic versus number r of Gaussian PDFs. Dashed lines indicate critical values which are set to one for normalized statistics; left and right transducers; data used at angles θ=62° (top) and θ=60° (bottom).

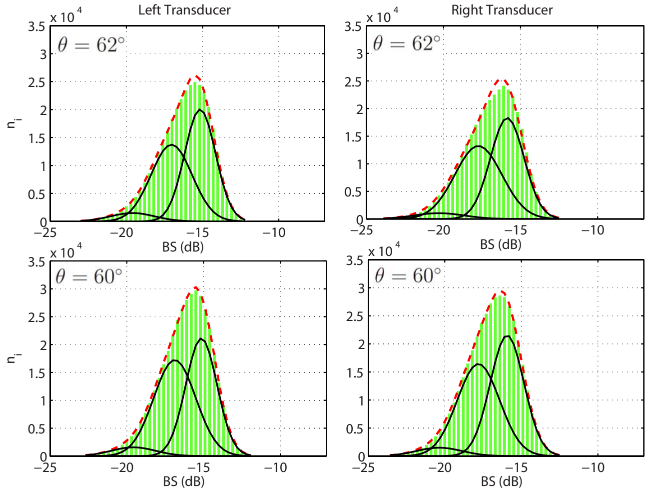

FIG. 7. (Color online) Histograms (light bar) of averaged (over small surface patches) backscatter data corrected for local slopes, its three Gaussians (solid line), and its best fit (dashed line) at angles θ=62° (top) and θ=60° (bottom) over the whole area; left and right transducers; number of Gaussians r=3.

dependent of the absolute values of the backscatter data. One may, for instance, think of the angular dependence of the backscatter data or the intrinsic difference between the backscatter data of the left and right transducers due to MBES transducer calibration effects.

To explore the full high-resolution mapping potential of the method, one may consider to use multiple beams instead of only one (Sec. III B, Step II). The ultimate goal of the acoustic classification method is to obtain a continuous map over the whole region, as for the bathymetry map. The classification map obtained from the averaged backscatter data using beam angles at θ=64°,62°, ... ,20° is shown in Fig. 8 in which the three sediment classes are presented by the colors red, yellow, and green. The green represents low values, the yellow represents intermediate values, and the red represents high values for the backscatter data. At a typical angle θ=60°, the acceptance regions are as follows: $[-\infty$ to $-18]$ dB (Class I), $[-18$ to $-16.25]$ dB (Class II), and $[-16.25$ to $+\infty]$ dB (Class III).

In general, a correlation between the bathymetry and the classification results is observed (Figs. 4 and 8); the deeper the depth is, the larger the backscatter values are, and hence the coarser the sediments will be. That is what we would expect, and intuitively ground truth the classification results (see Sec. V C). Note, however, that there exist also shallow water areas where the sediment is coarse grained (compare Fig. 4 with Fig. 8). That is an indication for the absence of any depth-dependent artifacts or unmodeled effects in the backscatter data.

To further elaborate on the performance of the classifi-

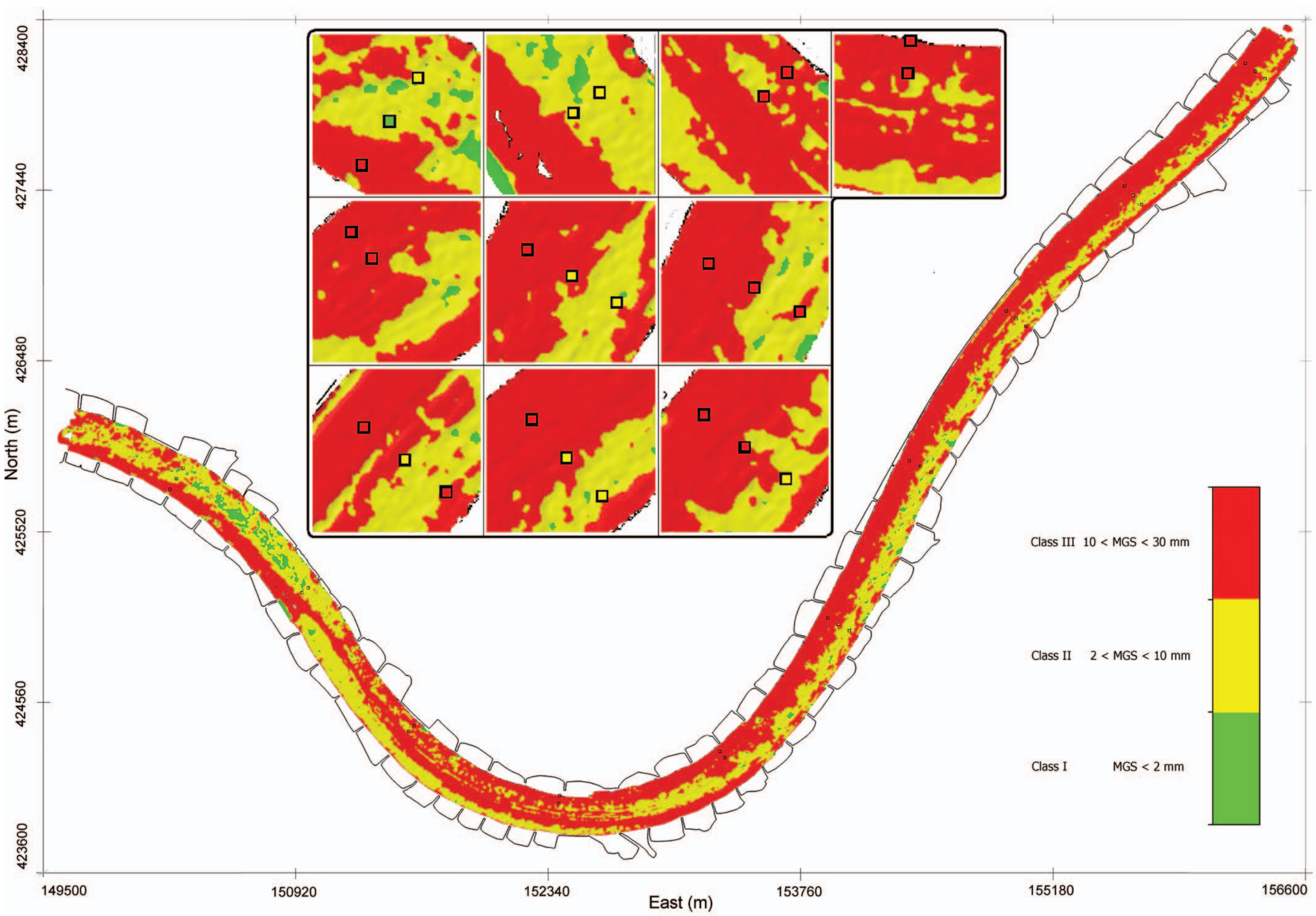

FIG. 8. Acoustic classification map of Waal river (km 920–930) obtained from backscatter at θ=64°,62°, ... ,20°. For each angle separate classification has been applied and results put in a single map. The frames on top indicate a zoom-in of classification results for areas where grab samples have been taken. A correlation of 0.75 is obtained between acoustic sediment classification and mean grain size from core analysis.

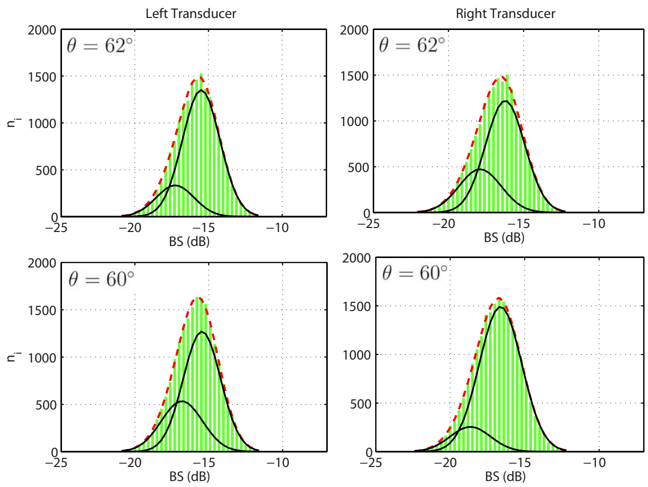

FIG. 9. (Color online) Histograms (light bar) of averaged (over small surface patches) backscatter data at θ=62° (top) and θ=60° (bottom) over the stable flat area; left and right transducers; number of Gaussians r=2.

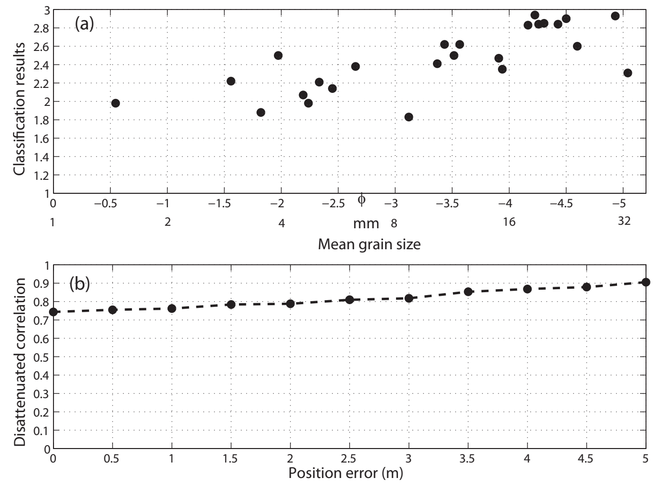

FIG. 10. Mean grain size from individual grab samples versus classification results (a). Disattenuated correlation coefficient (compensated for position error) between classification results and mean grain size of grabs (b). Note that ϕ scale has been inverted and positive correlation means that higher backscatter data are obtained over coarser sediment.

cation method, the averaged backscatter data over the southern part of a smaller area where the east component lies between 151 000 and 153 350 m—the stable flat area in Fig. 4—is now considered. The corresponding histogram along with two Gaussian PDFs is shown in Fig. 9. The left tails of the histograms are now shorter than those in Fig. 7. The two detected PDFs coincide with the results of the classification map using the three PDFs over the whole river (Fig. 8, two classes can be seen in this area).

C. Correlation with core analysis

The ultimate goal of MBES data analysis is to transform the backscatter classification results into estimates of seafloor sediment properties such as mean grain size. The goal of the sediment grab sampling and grain-size analysis is to evaluate the potential correlation between the mean grain size and the results from acoustic classification. A total number of 29 grab samples taken at the central axis of the river and at both sides (70 m apart from the central path) were collected and analyzed for grain-size distribution. There exist 25 samples which fall inside the survey area. The grab samples were washed, dried, and sieved through a series of mesh sizes ranging from 30 to 0.1 mm. The sieve sizes were converted into ϕ (phi) units[43] using the equation $\phi=-\log_2 d$, where d is diameter of grain in millimeters. Note that fine sediments have large ϕ values. Based on the comparison with the acoustic classification results, it can be concluded that the areas of high backscatter values correspond to gravel and lower backscatter values correspond to sand.

We now make a comparison between the classification results and the mean grain size of the samples. Our strategy is to use the results of the core analysis for comparison and to perform a correlation analysis afterward. The mean grain sizes were sorted from fine to coarse sediment. Considering the grab samples as an unbiased representative for the whole area, the percentages of 5%, 40%, and 55% were then applied to the 25 samples. This corresponds to 1, 10, and 14 samples, respectively for sand, gravelly sand, and sandy gravel areas. The classification results show good overall agreement with the ground truth information obtained from the core analysis [Fig. 8 zoom-in part, and Fig. 10(a)]. Most of the differences belong to the areas where the grab samples are in the boundary region of two classes. The dependence of acoustic backscatter techniques on sediment physical properties is examined using the Pearson correlation coefficient as well as a disattenuated correlation (Appendix B) between mean grain size of the samples and the classification results.

Due to the river currents' interaction with bottom sediments, the rivers are dynamic environments and hence sediment distribution can be highly heterogeneous. Ground truthing our classification results from core analysis of the sediments is prone to a few sources of uncertainty, of which we mention five. (i) Positioning error of the grab samples which is considered to be about 4–5 m: this issue is addressed in this section. (ii) The complexity inherent in ascertaining whether a single sample is representative of a larger region:[3] this originates from the heterogeneity of the river sediment distribution. (iii) A finite number of grab samples when assigning sediment types to acoustic classes, e.g., the percentage of the Class I (green) is 5% which leads to just one sample (if any) from 25 samples. (iv) Large standard deviation of backscatter data due to the shallowness of water, which leads to a small beam footprint: this has been accounted for, to a large extent, because of the averaging procedure. (v) Considering other physical properties of sediments rather than just the mean grain size. We can also use the full grain-size distribution and perform similar comparison.

We examine the potential correlation between classification results and the mean grain size. Larger grain sizes are expected to produce stronger backscatter for sandy and gravelly sediment. The Pearson correlation coefficient [Eq. (B7)] between the mean grain size and the results of the classification is 0.75. It indicates a high positive correlation (it is negatively correlated with ϕ values). The uncertainties (errors) mentioned above underestimate the correlation coefficient below the level it would have reached if the measurements had been precise. Such uncertainties can be accounted for in the correlation coefficient, which gives rise to the disattenuated correlation coefficient (see Appendix B). This correlation coefficient indicates whether the correlation between two data sets is low(er) because of measurement error or because the two sets are really uncorrelated. Therefore, if the measure for the uncertainties is available (for example, if it is estimated by an independent method), one can then obtain the disattenuated correlation coefficients.

To see how significantly the aforementioned effects impact the correlation coefficients, the effect of position errors of the samples is assessed. The disattenuated correlation is given by Eq. (B9), where its disattenuation coefficient λ is obtained from Eq. (B10). Based on the data themselves, one cannot estimate the measurement errors σ_{e_x} and σ_{e_y} (variation within the sub-populations). Variation in the sediment composition (due to sediment heterogeneity) versus position can be simulated using the classification results in the following way: (i) consider randomly a large number of points with their true positions and classification results, (ii) simulate the position error and add it up with the true position, (iii) look at the classification results at the simulated point, and (iv) obtain its difference with the classification results at the true positions and hence its standard deviation σ_{e_x}. A positive trend for the disattenuated correlation is observed versus position error [Fig. 10(b)]. The correlation coefficient, when taking the 5 m position error into account, increases from 0.75 to 0.90. Note, however, that the disattenuated correlation is an indication for the presence of measurement errors and not a substitute for precise measurements. Future work can use and apply a similar correlation analysis to the grain-size distribution of the sediments.

D. *K*-distributed backscatter intensity

1. Background

The classical Rayleigh distribution theory is not applicable when the number of scatterers within the signal footprint is not large enough to apply the central limit theorem. This theory is not applicable, at least, when (1) the seafloor and hence seafloor data are rough, (2) the number of scatterers within the signal footprint is not large enough, (3) the number of scatterers is a random variable with high variance, and (4) the assumption of independent and identically distributed scatterers is violated.

Statistical analysis of backscatter intensity typically deals with fitting a set of theoretical distributions to see which one describes the data best. Non-Rayleigh distributions can better fit the skewed distributions and provide new parameters for characterization. It is widely accepted to use the *K*-distribution when the classical Rayleigh distribution is not applicable to backscatter amplitudes.[24–27,29] The *K*-distribution is

$$f_I(I) = \frac{2\left(\frac{N\nu}{\mu}\right)^{(N+\nu)/2} I^{(N+\nu-2)/2}}{\Gamma(\nu)\Gamma(N)} K_{\nu-N}\left(2\sqrt{\frac{N\nu}{\mu}I}\right), \qquad (19)$$

where μ is the scale parameter, ν is the shape parameter, N is the multi-look parameter (i.e., the number of scatter pixels in the beam footprint), and $K_{\nu-N}$ is the modified Bessel function of the second kind. The *K*-distribution results from two independent Γ -distributed random variables. It has the advantage of being able to reproduce the classical distributions. For a given N, the *K*-distribution tends to the gamma distribution when the shape parameter increases to infinity ($\nu \to \infty$). In a special case when $N=1$, it then reduces to the exponential distribution.

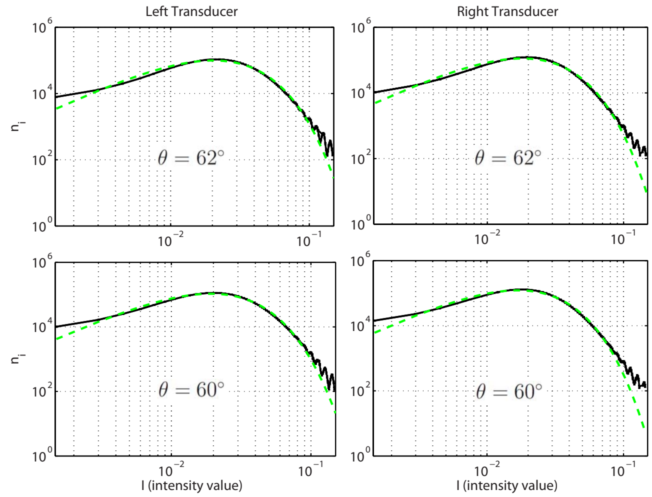

FIG. 11. (Color online) Measured histograms of backscatter intensity (solid black line) and statistical *K*-distribution (dashed light line) fitting; left and right transducers; θ=62° (top), θ=60° (bottom).

The maximum likelihood estimation method is usually applied to estimate the parameters μ and ν of the *K*-distribution.[44,45] An alternative is based on the method of moments.[46] We use a method which is based on the least-squares principle: fitting a curve to the histogram of the data in a least-squares sense (similar to Sec. III B, Step 1). Such estimates are first of all independent of the distribution of the data, second they are unbiased, and third they give the best possible precision (minimum variance) for the unknown parameters of the distribution.

The parameters μ and ν of the *K*-distribution depend on the incident angle. The *K*-distribution has proved to be a promising and useful model for the backscattering statistics in MBES and side-scan sonar data.[31,32] Also the *K*-distribution is of particular interest because its shape parameter is related to physical descriptors (e.g., spatial density of scatterers) of the seafloor.[29,30] Our application of the *K*-distribution is to further study the problem of riverbed characterization using the original backscatter intensities (without averaging). The angular evolution of the shape parameter ν is, in particular, investigated.

2. Results

The *K*-distribution is compared to the experimental PDF of the original backscatter intensities. Figure 11 shows typical graphical examples of the observed backscatter intensities along with their least-squares fit. The goodness of fit criterion [χ^2 values, similar to those in Eq. (3)] are as follows. For left transducer they are χ^2=242 and χ^2=209 at θ=62° and θ=60°, respectively. For right transducer they are χ^2=333 and χ^2=280 at θ=62° and θ=60°, respectively (see

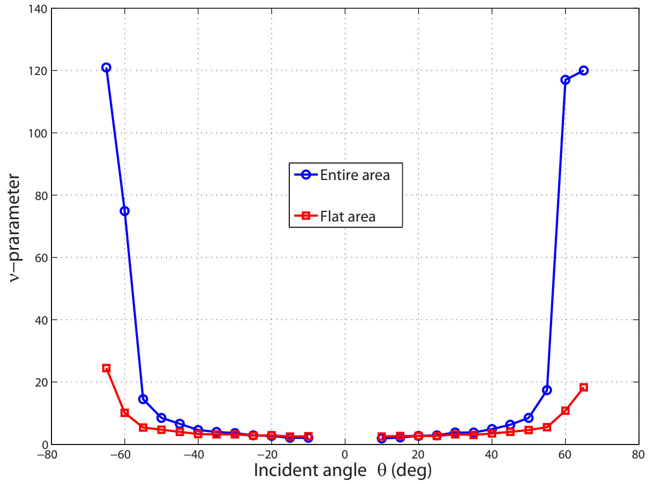

FIG. 12. (Color online) Angular evolution of shape parameter ν of K-distribution for entire area and flat area.

Fig. 6). The critical value is only 1.43. This indicates that the fit is not good enough because of large χ^2 values, which is a further indication for having more than one sediment types (this came out of the Gaussian fitting).

The angular evolution of backscattering statistics via the evolution of one parameter, the shape parameter ν in Eq. (19), of the K-distribution is now investigated. Its estimate is based on the least-squares curve fitting using the simultaneous estimation of the shape parameter ν and the scale parameter μ. The results for ν are shown in Fig. 12. The angular evolution of the shape parameter ν coincides with the findings of Refs. 31 and 32. For the intermediate incident angles, the shape-parameter values are low. At high incident (low grazing) angles, the increase is due to the extension of the beam footprint, which includes a greater number of scatterers; the central limit theorem applies, and the K-distribution tends to an exponential distribution (and correspondingly the Rayleigh distribution for amplitude).

The results given in Ref. 32 show a point where the functional behavior of the shape-parameter curves [i.e., $\nu = \nu(\theta)$] reverse for soft sediments, and that the rough seafloor does not seem to exhibit this transition angle. They indicate that the riverbed can be considered to be a rough surface (we cannot see such transition point here as the shape parameter increases with θ). We have already identified that the river sediment composition is formed primarily of coarse sand and gravel. This makes sense because the grain size of the sediment is a major contributor to the surface roughness.

We also observe that the shape parameters, in the stable flat area, are significantly smaller than their corresponding values in the entire area (Fig. 12). This can be considered as the effect of the bottom slopes, which is not seriously present in the flat area. The strong local slope variation as a normally distributed random variable will further increase the shape parameter of the K-distribution. Therefore, the K-distribution tends to an exponential distribution as in a Rayleigh reverberation process.

VI. SUMMARY AND CONCLUSIONS

Riverbed sediment classification using MBESs, backscatter data is a promising approach. The degree to which different bottom types can be discriminated using the backscatter data depends on the following. (i) Geoacoustical features of the bottom types: an obvious effect is on the mean and variance of the backscatter data. (ii) Measurement configuration such as beam grazing angle, water depth, pulse length, and number of scatterers in the signal footprint: such issues usually affect the distribution of the backscatter data. (iii) The presence of local slopes of the seafloor. In principle, the backscatter data should be corrected for bottom slopes. The differential slopes might, however, significantly affect the distribution parameters.

This contribution presented a methodology to use the (very) high-frequency MBES backscatter data for the sediment classification in very shallow water applications (depth of 2–10 m). The MBES used is an EM3002, typically working at 300 kHz with the maximum 254 number of beams. However, there is no restriction regarding the capability of the method for other water depths and frequencies. This method employs the MBES backscatter data to obtain the number of classes and to discriminate between them by applying the Bayes decision rule for multiple hypotheses. This is achieved by fitting a series of Gaussian PDFs to the backscatter strength histogram. Since the classification is done per beam, the method is independent of the possible incorrect calibration effects and the angular behavior of the backscatter data.

The performance of the method was tested by using the backscatter data acquired in the river Waal, The Netherlands. Extensive sediment grab samples analyzed for the grain-size distribution were used to evaluate the performance of the classification results. The following aspects of the research are highlighted.

- Shallow water depths result in small beam footprints and hence a small number of scatter pixels per beam. That makes the backscatter data highly variable and consequently the classification method becomes less efficient. To increase the discriminating power of the classification results, we used an averaging procedure over small surface patches 0.5×0.5 m^2. The high resolution bathymetry data provide precise bottom slope corrections to convert the arrival angle of the signal into the true incident angle, and the high resolution backscatter data allow one to reduce the statistical fluctuation in backscatter strength.
- We performed a correlation analysis. The dependence of acoustic backscatter classification on sediment physical properties was verified by using Pearson (0.75) and disattenuated (0.90) correlation coefficients between the classification results and sediment mean grain size. The disattenuated correlation gives an indication for the effects of measurement errors that attenuate the correlation below the level it would have reached had the measurements been precise.
- We considered the backscattered intensity statistics using the K-distribution to further study the riverbed characterization. Angular evolution of the K-distribution shape parameter indicated that the Waal riverbed is indeed a rough surface. It is in agreement with the ground truth information from the core analysis.

ACKNOWLEDGMENTS

The research is financially supported by the Dutch Ministry of Transportation and Water Management, Rijkswaterstaat. We acknowledge, in particular, Dr. Arjan Sieben, Ir. Ben Dierikx, and Adri Wagener for providing the Waal data and for their support during this project. We would also like to acknowledge the associate editor and two anonymous reviewers for their constructive comments which improved the presentation and quality of the paper.

APPENDIX A: COORDINATE TRANSFORMATION

The linear model of observation equations in the vessel coordinate system x-y is

$$E(z) = Aa, \tag{A1}$$

where z is the bathymetry data, A is the $m \times 6$ design matrix of the form

$$A = [1\ X\ Y\ X^2\ Y^2\ XY], \tag{A2}$$

or, written out as

$$A = \begin{bmatrix} 1 & x_1 & y_1 & x_1^2 & y_1^2 & x_1y_1 \\ \vdots & \vdots & \vdots & \vdots & \vdots & \vdots \\ 1 & x_m & y_m & x_m^2 & y_m^2 & x_my_m \end{bmatrix}, \tag{A3}$$

and a is the unknown coefficients of the bi-quadratic polynomial. The least-squares estimate of a is

$$\hat{a} = (A^TQ_z^{-1}A)^{-1}A^TQ_z^{-1}z. \tag{A4}$$

Another parametrization of the above system of observation equations is based on the UTM coordinate system (north N and east E)

$$E(z) = A'a', \tag{A5}$$

where

$$A' = [1\ N\ E\ N^2\ E^2\ NE]. \tag{A6}$$

The prime $'$ indicates that the terms are now defined in the new coordinate system. The least-squares estimate for a' is

$$\hat{a}' = (A'^TQ_z^{-1}A')^{-1}A'^TQ_z^{-1}z. \tag{A7}$$

One can simply show that the design matrices A and A' are related using the transformation $A=A'T$, where T is a 6×6 regular matrix of the form

$$T = \begin{bmatrix} 1 & 0 & 0 & 0 & 0 & 0 \\ 0 & \cos\alpha & -\sin\alpha & 0 & 0 & 0 \\ 0 & \sin\alpha & \cos\alpha & 0 & 0 & 0 \\ 0 & 0 & 0 & \cos^2\alpha & \sin^2\alpha & \frac{-1}{2}\sin 2\alpha \\ 0 & 0 & 0 & \sin^2\alpha & \cos^2\alpha & \frac{1}{2}\sin 2\alpha \\ 0 & 0 & 0 & \sin 2\alpha & -\sin 2\alpha & \cos 2\alpha \end{bmatrix}, \tag{A8}$$

with the inverse

$$T^{-1} = \begin{bmatrix} 1 & 0 & 0 & 0 & 0 & 0 \\ 0 & \cos\alpha & \sin\alpha & 0 & 0 & 0 \\ 0 & -\sin\alpha & \cos\alpha & 0 & 0 & 0 \\ 0 & 0 & 0 & \cos^2\alpha & \sin^2\alpha & \frac{1}{2}\sin 2\alpha \\ 0 & 0 & 0 & \sin^2\alpha & \cos^2\alpha & \frac{-1}{2}\sin 2\alpha \\ 0 & 0 & 0 & -\sin 2\alpha & \sin 2\alpha & \cos 2\alpha \end{bmatrix}, \tag{A9}$$

where α is the heading angle of the vessel. Substituting $A = A'T$ in Eq. (A4) gives the relation between the least-squares estimates $\hat{a}$ and $\hat{a}'$ as

$$\hat{a} = T^{-1}(A'^TQ_z^{-1}A')^{-1}A'^TQ_z^{-1}z = T^{-1}\hat{a}' \tag{A10}$$

or

$$\begin{bmatrix} \hat{a}_0 \\ \hat{a}_1 \\ \hat{a}_2 \\ \hat{a}_3 \\ \hat{a}_4 \\ \hat{a}_5 \end{bmatrix} = \begin{bmatrix} \hat{a}'_0 \\ \hat{a}'_1\cos\alpha + \hat{a}'_2\sin\alpha \\ \hat{a}'_2\cos\alpha - \hat{a}'_1\sin\alpha \\ \hat{a}'_3\cos^2\alpha + \hat{a}'_4\sin^2\alpha + \frac{1}{2}\hat{a}'_5\sin 2\alpha \\ \hat{a}'_3\sin^2\alpha + \hat{a}'_4\cos^2\alpha - \frac{1}{2}\hat{a}'_5\sin 2\alpha \\ \hat{a}'_4\sin 2\alpha - \hat{a}'_3\sin 2\alpha + \hat{a}'_5\cos 2\alpha \end{bmatrix}. \tag{A11}$$

Equations $\hat{a}_x=\hat{a}_1+2\hat{a}_3x+\hat{a}_5y$ and $\hat{a}_y=\hat{a}_2+2\hat{a}_4y+\hat{a}_5x$ with $x=N\cos\alpha+E\sin\alpha$, $y=E\cos\alpha-N\sin\alpha$, and Eq. (A11) simplify to

$$\hat{a}_x = (\hat{a}'_1 + 2\hat{a}'_3N + \hat{a}'_5E)\cos\alpha + (\hat{a}'_2 + 2\hat{a}'_4E + \hat{a}'_5N)\sin\alpha, \tag{A12}$$

$$\hat{a}_y = (\hat{a}'_2 + 2\hat{a}'_4E + \hat{a}'_5N)\cos\alpha - (\hat{a}'_1 + 2\hat{a}'_3N + \hat{a}'_5E)\sin\alpha, \tag{A13}$$

or simply

$$\hat{a}_x = \hat{a}_N\cos\alpha + \hat{a}_E\sin\alpha, \tag{A14}$$

$$\hat{a}_y = \hat{a}_E\cos\alpha - \hat{a}_N\sin\alpha, \tag{A15}$$

where $\hat{a}_N=\hat{a}'_1+2\hat{a}'_3N+\hat{a}'_5E$ and $\hat{a}_E=\hat{a}'_2+2\hat{a}'_4E+\hat{a}'_5N$ are the estimated slopes in the north and east directions, respectively.

APPENDIX B: DISATTENUATED CORRELATION COEFFICIENT

Consider the data set $x=[x_1,\ldots,x_m]^T$ and $y=[y_1,\ldots,y_m]^T$, as a realization of the following random variables: $\underline{x}_i=\mu_x+\epsilon_{x_i}+e_{x_i}$ and $\underline{y}_i=\mu_y+\epsilon_{x_i}+e_{y_i}$, where the μ's represent the mean values, the ϵ's represent variation *between* sub-population, and the e's represent variation *within* the sub-populations (measurement error). The underline indicates randomness. The variances of the components ϵ_{x_i}, ϵ_{y_i}, e_{x_i}, and e_{y_i} are assumed to be $\sigma^2_{\epsilon_x}$, $\sigma^2_{\epsilon_y}$, $\sigma^2_{e_x}$, and $\sigma^2_{e_y}$, respectively. The ϵ_x and ϵ_y are assumed to be correlated ($\sigma_{\epsilon_x\epsilon_y} \neq 0$), but the measurement errors e_x and e_y are assumed to be uncorrelated ($\sigma_{e_xe_y}=0$). The above formulas can be written in a matrix notation as

$$\begin{bmatrix} \underline{x} \\ \underline{y} \end{bmatrix} = \begin{bmatrix} \mu_x \\ \mu_y \end{bmatrix} + \begin{bmatrix} 1 & 0 & 1 & 0 \\ 0 & 1 & 0 & 1 \end{bmatrix} \begin{bmatrix} \epsilon_x \\ \epsilon_y \\ e_x \\ e_y \end{bmatrix}, \tag{B1}$$

with the covariance matrix of

$$D\left\{\begin{bmatrix} \epsilon_x \\ \epsilon_y \\ e_x \\ e_y \end{bmatrix}\right\} = \begin{bmatrix} \sigma^2_{\epsilon_x} & \sigma_{\epsilon_x\epsilon_y} & 0 & 0 \\ \sigma_{\epsilon_x\epsilon_y} & \sigma^2_{\epsilon_y} & 0 & 0 \\ 0 & 0 & \sigma^2_{e_x} & 0 \\ 0 & 0 & 0 & \sigma^2_{e_y} \end{bmatrix}. \tag{B2}$$

Application of the variance propagation law[47] gives the covariance matrix of $[\underline{x},\underline{y}]^T$ as

$$D\left\{\begin{bmatrix} \underline{x} \\ \underline{y} \end{bmatrix}\right\} = \begin{bmatrix} \sigma^2_{\epsilon_x} + \sigma^2_{e_x} & \sigma_{\epsilon_x\epsilon_y} \\ \sigma_{\epsilon_x\epsilon_y} & \sigma^2_{\epsilon_y} + \sigma^2_{e_y} \end{bmatrix}. \tag{B3}$$

If we have a series of m samples of random variables x and y, written as x_i and y_i, where $i=1,\ldots,m$, then the variances $\sigma_x^2=\sigma^2_{\epsilon_x}+\sigma^2_{e_x}$ and $\sigma_y^2=\sigma^2_{\epsilon_y}+\sigma^2_{e_y}$ and the covariance $\sigma_{xy}=\sigma_{\epsilon_x\epsilon_y}$ can be estimated using the following linear model of observation equations:

$$E\left\{\begin{bmatrix} \underline{x} \\ \underline{y} \end{bmatrix}\right\} = \begin{bmatrix} u & 0 \\ 0 & u \end{bmatrix} \begin{bmatrix} \mu_x \\ \mu_y \end{bmatrix}, \tag{B4}$$

with the covariance matrix

$$D\left\{\begin{bmatrix} \underline{x} \\ \underline{y} \end{bmatrix}\right\} = \begin{bmatrix} \sigma_x^2 I & \sigma_{xy} I \\ \sigma_{xy} I & \sigma_y^2 I \end{bmatrix}, \tag{B5}$$

where $u=[1,1,\ldots,1]^T$ is a summation vector. The least-squares estimates of σ_x^2, σ_y^2, and σ_{xy} are then[40,48]

$$\begin{aligned} \hat{\sigma}_x^2 &= (x-\bar{x})^T(x-\bar{x})/(m-1), \\ \hat{\sigma}_y^2 &= (y-\bar{y})^T(y-\bar{y})/(m-1), \\ \hat{\sigma}_{xy} &= (x-\bar{x})^T(y-\bar{y})/(m-1), \end{aligned} \tag{B6}$$

where $\bar{x}=(1/m)\Sigma_{i=1}^m x_i$ and $\bar{y}=(1/m)\Sigma_{i=1}^m y_i$ are the sample means. The Pearson correlation coefficient (sample correlation) can then be used to estimate the correlation between x and y:[49]

$$\rho_{xy} = \frac{\hat{\sigma}_{xy}}{\sqrt{\hat{\sigma}_x^2 \hat{\sigma}_y^2}} = \frac{\hat{\sigma}_{\epsilon_x\epsilon_y}}{\sqrt{(\hat{\sigma}^2_{\epsilon_x} + \hat{\sigma}^2_{e_x})(\hat{\sigma}^2_{\epsilon_y} + \hat{\sigma}^2_{e_y})}}. \tag{B7}$$

When two data sets x and y are correlated, measurement errors underestimate the correlation coefficient. Measurement error can be accounted for in a correlation coefficient, which gives rise to the correlation coefficient disattenuated of measurement error

$$\rho^d_{xy} = \frac{\hat{\sigma}_{\epsilon_x\epsilon_y}}{\sqrt{\hat{\sigma}^2_{\epsilon_x}\hat{\sigma}^2_{\epsilon_y}}}. \tag{B8}$$

Disattenuated correlation coefficient indicates whether the correlation between two data sets is low because of measurement error or because the two sets are really uncorrelated. Note that Eq. (B6) gives $\hat{\sigma}_x^2$ and $\hat{\sigma}_y^2$, and not separately $\hat{\sigma}^2_{\epsilon_x}$, $\hat{\sigma}^2_{e_x}$, $\hat{\sigma}^2_{\epsilon_y}$, and $\hat{\sigma}^2_{e_y}$. If the measurement errors are available (for example, if they are estimated by an independent tool such as simulation), one can account for them and obtain the disattenuated correlation coefficients. The relation between Pearson correlation coefficient and its disattenuated one is

$$\rho_{xy} = \lambda \rho^d_{xy}, \tag{B9}$$

where λ is the attenuation coefficient

$$\lambda = \frac{\sigma_{\epsilon_x}\sigma_{\epsilon_y}}{\sqrt{(\sigma^2_{\epsilon_x} + \sigma^2_{e_x})(\sigma^2_{\epsilon_y} + \sigma^2_{e_y})}}. \tag{B10}$$

How well the variables are measured affects the correlation of x and y. The correction for attenuation shows the correlation as if one measures x and y without errors.

[1] X. Lurton, *An Introduction to Underwater Acoustics: Principles and Applications* (Springer, New York, 2002), pp. 90–91.

[2] D. G. Simons and M. Snellen, "A Bayesian approach to seafloor classification using multi-beam echo-sounder backscatter data," Appl. Acoust. **70**, 1258–1268 (2009).

[3] J. A. Goff, H. C. Olson, and C. S. Duncan, "Correlation of side-scan backscatter intensity with grain-size distribution of shelf sediments, New Jersey margin," Geo-Mar. Lett. **20**, 43–49 (2000).

[4] J. S. Collier and C. J. Brown, "Correlation of sidescan backscatter with grain size distribution of surficial seabed sediments," Mar. Geol. **214**, 431–449 (2005).

[5] J. C. Borgeld, J. E. Hughes Clarke, J. A. Goff, L. A. Mayer, and J. A. Curtis, "Acoustic backscatter of the 1995 flood deposit on the Eel shelf," Mar. Geol. **154**, 197–210 (1999).

[6] R. Urgeles, J. Locat, T. Schmitt, and J. E. Hughes Clarke, "The July 1996 flood deposit in the Saguenay Fjord, Quebec, Canada: Implications for sources of spatial and temporal backscatter variations," Mar. Geol. **184**, 41–60 (2002).

[7] V. L. Ferrini and R. D. Flood, "The effects of fine-scale surface roughness and grain size on 300 kHz multibeam backscatter intensity in sandy marine sedimentary environments," Mar. Geol. **228**, 153–172 (2006).

[8] D. G. Simons, M. Snellen, and M. Ainslie, "A multivariate correlation analysis of high-frequency bottom backscattering strength measurements with geotechnical parameters," IEEE J. Ocean. Eng. **32**, 640–650 (2007).

[9] T. Medialdea, L. Somoza, R. León, M. Farrán, G. Ercilla, A. Maestro, D. Casas, E. Llave, F. J. Hernández-Molina, M. C. Fernández-Puga, and B. Alonso, "Multibeam backscatter as a tool for sea-floor characterization and identification of oil spills in the Galicia Bank," Mar. Geol. **249**, 93–107 (2008).

[10] D. Alexandrou and D. Pantzartzis, "A methodology for acoustic seafloor classification," IEEE J. Ocean. Eng. **18**, 81–86 (1993).

[11] Z. H. Michalopoulou, D. Alexandrou, and C. de Moustier, "Application of neural and statistical classifiers to the problem of seafloor characterization," IEEE J. Ocean. Eng. **20**, 190–197 (1995).

[12] I. Marsh and C. Brown, "Neural network classification of multibeam backscatter and bathymetry data from Stanton Bank (Area IV)," Appl. Acoust. **70**, 1269–1276 (2009).

[13] L. Fonseca and L. Mayer, "Remote estimation of surficial seafloor properties through the application angular range analysis to multibeam sonar data," Mar. Geophys. Res. **28**, 119–126 (2007).

[14] L. Fonseca, C. Brown, B. Calder, L. Mayer, and Y. Rzhanov, "Angular range analysis of acoustic themes from Stanton Banks Ireland: A link between visual interpretation and multibeam echosounder angular signatures," Appl. Acoust. **70**, 1298–1304 (2009).

[15] X. Zhou and Y. Chen, "Seafloor classification of multibeam sonar data using neural network approach," Mar. Geodesy **28**, 201–206 (2005).

[16] J. Hughes Clarke, "Toward remote seafloor classification using the angular response of acoustic backscattering: A case study from multiple overlapping GLORIA data," IEEE J. Ocean. Eng. **19**, 112–127 (1994).

[17] I. M. Parnum, A. N. Gavrilov, P. J. W. Siwabessy, and A. J. Duncan, "Analysis of high-frequency multibeam backscatter statistics from different seafloor habitats," in *Proceedings of the Eighth European Conference*

on Underwater Acoustics, Carvoeiro, Portugal (2006), pp. 1020–1031.
[18] G. S. Brown, "Backscattering from Gaussian-distributed perfectly conducting rough surface," IEEE Trans. Antennas Propag. **AP-26**, 472–482 (1978).
[19] F. T. Ulaby, T. F. Haddock, and R. T. Austin, "Fluctuation statistics of millimeter-wave scattering from distributed targets," IEEE Trans. Geosci. Remote Sens. **26**, 268–281 (1988).
[20] M. Gensane, "A statistical study of acoustic signals backscattered from the sea bottom," IEEE J. Ocean. Eng. **14**, 84–93 (1989).
[21] E. Jakeman and P. N. Pusey, "A model for non-Rayleigh sea echo," IEEE Trans. Antennas Propag. **AP-24**, 806–814 (1976).
[22] E. Jakeman and P. N. Pusey, "Significance of K-distributions in scattering experiments," Phys. Rev. Lett. **40**, 546–550 (1978).
[23] C. J. Oliver, "A model for non-Rayleigh scattering statistics," Opt. Acta **31**, 701–722 (1984).
[24] E. Jakeman, "Non-Gaussian models for the statistics of the scattered waves," Adv. Phys. **37**, 471–529 (1988).
[25] C. J. Oliver, "Correlated K-distributed clutter models," Opt. Acta **32**, 1515–1547 (1985).
[26] J. Dunlop, "Statistical modeling of sidescan sonar images," in *Oceans Conference Record (IEEE)*, Piscataway, NJ (1997), Vol. **1**, pp. 33–37.
[27] A. P. Lyons and D. A. Abraham, "Statistical characterization of high-frequency shallow-water seafloor backscatter," J. Acoust. Soc. Am. **106**, 1307–1315 (1999).
[28] F. P. A. Lam, N. J. Konijnendijk, J. Groen, and D. G. Simons, "Non-Rayleigh wideband sonar reverberation modeling including hybrid multipaths," in *Proceedings of the MTS/IEEE Oceans'06*, Boston, MA, edited by M. Prior and D. Abraham (IEEE Operations Center, Piscataway, NJ, 2006).
[29] D. A. Abrahams and A. P. Lyons, "Novel physical interpretations of K-distributed reverberation," IEEE J. Ocean. Eng. **27**, 800–813 (2002).
[30] M. K. Prior, "Estimation of K-distribution shape parameter from sonar data: Sample size limitations," IEEE J. Ocean. Eng. **34**, 45–50 (2009).
[31] L. Hellequin and J. M. Boucher, "Processing of high-frequency multibeam echo sounder data for seafloor characterization," IEEE J. Ocean. Eng. **28**, 78–89 (2003).
[32] G. Le Chenadec and J. M. Boucher, "Angular dependence of *K*-distributed sonar data," IEEE Trans. Geosci. Remote Sens. **45**, 1224–1235 (2007).
[33] E. J. Gumbel, *Statistics of Extremes* (Columbia University Press, New York, 1958).
[34] R. A. Fisher and L. H. C. Tippett, "Limiting forms of the frequency distribution of the largest and smallest member of a sample," Proc. Cambridge Philos. Soc. **24**, 180–190 (1928).
[35] T. F. Coleman and Y. Li, "An interior trust region approach for nonlinear minimization subject to bounds," SIAM J. Optim. **6**, 418–445 (1996).
[36] C. L. Lawson and R. J. Hanson, *Solving Least-Squares Problems* (Prentice-Hall, Englewood Cliffs, NJ, 1974).
[37] J. A. Goff, B. J. Kraft, L. A. Mayer, S. G. Schock, C. K. Sommerfield, H. C. Olson, S. P. S. Gulick, and S. Nordfjord, "Seabed characterization on the New Jersey middle and outer shelf: Correlatability and spatial variability of seafloor sediment properties," Mar. Geol. **209**, 147–172 (2004).
[38] FLEDERMAUS software: Interactive visualization systems (IVS 3D), a 3D visualization and analysis software, http://www.ivs3d.com/ (Last viewed 3/31/09).
[39] P. J. G. Teunissen, *Testing Theory: An Introduction* (Delft University Press, Delft, The Netherlands, 2000), pp. 132–136, http://www.vssd.nl/hlf/landmeet.html (Last viewed 7/12/09).
[40] A. R. Amiri-Simkooei, "Least-squares variance component estimation: Theory and GPS applications," Ph.D. thesis, Delft University of Technology, Delft, The Netherlands (2007).
[41] P. J. G. Teunissen, *Adjustment Theory: An Introduction* (Delft University Press, Delft, The Netherlands, 2000), pp. 178–191, http://www.vssd.nl/hlf/landmeet.html (Last viewed 7/12/09).
[42] International Committee of the hydrology of the Rhine basin (CHR), basin of the Rhine, Hydrological monograph, CHR/KHR, The Hague, The Netherlands, 1977.
[43] C. K. Wentworth, "A scale of grade and class terms for clastic sediments," J. Geol. **30**, 377–392 (1922).
[44] C. J. Oliver, "Optimum texture estimators for SAR clutter," J. Phys. D: Appl. Phys. **26**, 1824–1835 (1993).
[45] I. R. Joughin, D. B. Percival, and D. P. Winebrenner, "Maximum likelihood estimation of K distribution parameters for SAR data," IEEE Trans. Geosci. Remote Sens. **31**, 989–999 (1993).
[46] C. J. Oliver, "Information from SAR images," J. Phys. D **24**, 1493–1514 (1991).
[47] P. J. G. Teunissen, D. G. Simons, and C. C. J. M. Tiberius, *Probability and Observation Theory* (Delft University, Delft, The Netherlands, 2005).
[48] P. J. G. Teunissen and A. R. Amiri-Simkooei, "Least-squares variance component estimation," J. Geodesy, Berlin **82**, 65–82 (2008).
[49] W. H. Press, B. P. Flannery, S. A. Teukolsky, and W. T. Vetterling, *Numerical Recipes* (Cambridge University Press, New York, 1992).